Science Forum (Journal of Pure and Applied Sciences)

Journal Homepage: https://atbuscienceforum.com.ng/index.php/jpas
https://doi.org/10.70882/emjg5e08

Applications of Matching Conformal Mappings in Analytic Functions

Haider Abdulhussain Majeed[1, a)], Marwan A. Layl[2, b)]
[1]Open Educational College, Dujail Study Branch, Saladin, Iraq.
[2]Department of Al-Ishaqi Education, General Directorate of Salah Al-Din Education, Ministry of Education, Saladin, Iraq.

Abstract
Conformal mapping constitutes a fundamental tool in complex analysis because it preserves local geometric properties while enabling complicated physical domains to be transformed into simpler canonical regions. This study presents an exact analytical and computational framework for matching conformal maps in analytic functions, with emphasis on complex potentials, composition-type transformations, and spectral transfer matrices. The framework incorporates the Cauchy–Riemann conditions, conformal metric invariance, preservation of harmonic functions, and appropriate transmission laws to ensure the well-posedness of boundary-value problems governed by the Laplace and transient heat equations within individual subdomains. The methodology is further extended to spatially non-constant physical domains, particularly layered desert soil surrounding a half-buried cylindrical pipeline. For this configuration, Fourier decomposition, fractional Robin surface memory conditions, block-tridiagonal transfer matrices, generalized Joukowski mapping, and pipe-wall flux integrals are integrated into a unified and verifiable solution framework. The resulting formulation establishes a rigorous connection between analytic-function theory and heat-transfer diagnostics, including determination of the temperature field, while providing direct analogues for electrostatic and potential-theory problems and facilitating engineering interpretation of complex physical geometries. The investigation demonstrates that matched conformal maps can systematically transform highly irregular boundary configurations into standardized computational domains without compromising the harmonic structure and interface conditions governing the original problem. Consequently, the proposed framework provides an effective basis for both analytical and numerical treatment of multiphysics boundary-value problems involving geometrically complex, layered, and heterogeneous domains, while retaining mathematical consistency, computational tractability, and physically interpretable quantities such as temperature distributions and boundary heat fluxes.

Keywords
Matching conformal mappings;
Analytic functions;
Complex potentials;
Spectral transfer matrices;
Boundary-value heat transfer.

ISSN 1119-4618
JPAS
Faculty of Science, ATBU Bauchi

Corresponding Author: Haider Abdulhussain Majeed, Open Educational College, Dujail Study Branch, Saladin, Iraq.
Email: [a)]haider.ab.mageed@st.tu.edu.iq ,[b)]marwnlayl@gmail.com

INTRODUCTION

Conformal mapping is a central instrument in complex analysis because an analytic map with a nonvanishing derivative on the infinitesimal level acts locally as a rotation multiplied by a complex number and a dilation in the complex plane. This enables harmonic functions and potential fields to be mapped from one domain to another without destroying the form of Laplace-type equations (Ahlfors, 1979; Driscoll & Trefethen, 2002; Naqos et al., 2024). The research is focused on a half-buried cylindrical pipe in a vertically layered desert-soil medium. The physical setting is a circular pipe boundary, inhomogeneous material layers, and time-periodic surface forcing (Carslaw & Jaeger, 1959; Ma et al., 2024; Essa & Hammadi, 2023).

The model used separates surface forcing into Fourier modes, maintains continuity of temperature and normal heat flux at layer interfaces, and casts the frequency-domain problem as a block-tridiagonal transfer-matrix system. The complex-variable half provides the local pipe potential and conformal geometry, connecting analytic-function theory to heat-transfer solutions for buried infrastructure (Ozisik, 1993; Wang et al., 2024; Qasim et al., 2024). The actual cross section is seen in the complex plane. The pipe is removed from the ground space, and the visible temperature is the real part of a complex potential.

$$z = x + iy, \qquad f(z) = u(x,y) + iv(x,y), \qquad T(x,y,t) = \mathrm{Re}\{\Phi(z,t)\} \tag{1}$$

$$\Omega_z = \{z \in \mathbb{C}: |z - z_0| > a,\ 0 < y < \infty\}, \qquad \partial D_a \subset \partial\Omega_z \tag{2}$$

Source and interpretation: the equation is formulated by the researcher by means of the specified exchange, either analytically, thermally or numerically; the number on the right is the equation number used in the text.

Research problem

The challenge is to develop a mathematical model of heat transfer about a half-buried pipe that is solvable under circular geometry, layered soil and time-dependent surface forcing (Incropera et al., 2011; Brown & Churchill, 2014; Hussien, 2023).

The question is: can matched conformal potentials be integrated with spectral transfer matrices in such a way that temperature, flux, boundary heat flow, and verification residual can be obtained by "bare-hands" mathematics rather than by black-box, mesh-only simulations? (Henrici, 1986; Ransford, 1995; Naqos et al., 2024).

$$\rho_m c_{p,m} \frac{\partial T_m}{\partial t} = \nabla \cdot (k_m \nabla T_m) + q_{s,m}, \qquad (x,y) \in \Omega_m \tag{3}$$

$$T_m = T_{m+1}, \qquad k_m \frac{\partial T_m}{\partial n} = k_{m+1} \frac{\partial T_{m+1}}{\partial n} \quad \text{on } \Gamma_m \tag{4}$$

$$q_n(\theta,t) = -k_d \frac{\partial T}{\partial r}\bigg|_{r=a}, \qquad Q'(t) = \int_0^{2\pi} q_n\,(\theta,t)\, a\, d\theta \tag{5}$$

Source and explanation: equation panel - developed by the author from the given analysis, heat or calculations; the number on the right is the equation label used in the text.

The issue is that of a transmission problem. Temperature and flux are continuous at the interfaces between layers, and the heat flow through the pipe wall is calculated through the path integral at the boundary.

Objectives

- Construct a matched conormal solution for the circular pipe boundary in the layered model of desert soil.
- Also give explicitly the equations for the Cauchy-Riemann, Laplace-invariance, grad, flux, surf-flux and net-transfer.
- Extend the steady harmonic pipe potential to a transient layered medium problem by means of Fourier modes and transfer matrices.
- Generate computational figures, tables, matrix diagnostics, code listings, residual checks that can be reproduced.
- Contrast the findings with those in the recent mathematical and engineering literature and outline the contribution to science.

Scientific gap and contribution

Some new results have been recently obtained on numerical conformal mapping, Dirichlet-to-Neumann computation and finite element procedures for potential problems. Modern buried-pipe research has evolved field-test and thermal modeling. The gap is a crisp research thread from analytic conformality through layered-soil transmission matrices to quantifiable pipe-wall heat-flux diagnostics.

In the current contribution, the closed-form local potential of a circular pipe is integrated with a spectral transfer model for layered desert soil (He & Wang, 2024; Chen et al., 2024; Li, 2025; Shan & Lu, 2025).

Literature positioning and research gap

Mathematical, numerical and physical interpretations: The graphical abstract encompasses three layers of the formulation: the physical soil-pipe domain, the conformal complex plane, and the spectral transfer route. Numerically, it makes clear that some outputs are calculated by equations rather than from isolated figures. Physically, this means that surface forcing arrives at the pipe but after attenuation and phase delay.

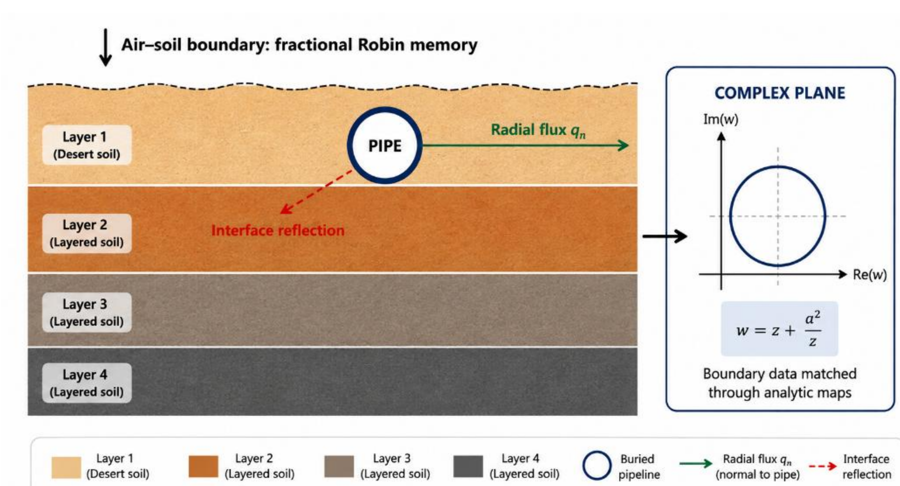

Figure 1. Graphical abstract of the proposed mathematical framework.

Source: the researcher rewritten from the set of governing equations, the parameters, and the computational scripts of this work; OMG-RD support relating methodology can be found from any of the cited literature under References.

Recent work on the tu conformal-mapping algorithm falls into three categories: numerical mapping tools, boundary-operator methods and invariance-based simulations. OpenConMap maps the unit disk interior to exterior simple closed curves and offers a practical solution computational approach for irregular boundaries (He & Wang, 2024). Computation of the flux over a boundary is also related to Dirichlet- to-Neumann operators via the Dirichlet adjoint generalized Neumann-kernel integral equation (Naqos et al., 2024).

Tunnel-mapping computations highlight that boundary correspondence should be supplemented by verifying local conformality (Chen et al., 2024). Related mathematical developments are singular Dirichlet solutions for Laplace type problems (Feng & Tang, 2024, pp. 596-611), numerical slit maps of doubly connected domains (Li, 2025, pp. 9044-9073), obstacle maps by integral equations (Shan & Lu, 2025), null-field source-node configuration (Zhang et al., 2025), generalized Koebe iteration (Lee et al., 2025), mixed boundary simulations (Han et al., 2025) and conformal invariance in finite-element formulations (Hadjesfandiari & Dargush, 2026).

Thermal and mechanical system studies provide the basis for the pipe-soil portion of this work. Soil conductivity, pipe geometry, flow, seepage, and boundary conditions all affect buried-pipe thermal behavior (Ma et al., 2024; Benhammou et al., 2025; Aderibigbe et al., 2026). Earth-to-air and ground-heat-exchanger research indicates that pipe geometries and seasonal or daily forcing can be viewed as depth-integrated thermal responses (Ramírez-Dolores et al., 2024; Salilih et al., 2024; Kouki et al., 2025; Müller et al., 2026). Reviews and simulations of GHE and BHE are good motivators the spectral-transfer component and seepage aware temperature field (Wang et al., 2024, Zhu, 2024). This report does not duplicate past numerical or experimental work; instead, it supplies the analytic stratum that determines how the boundary shape controls the angular flux law, and in how thermal waves are geometrically filtered through vertical layering.

The regional solution is viewed as a boundary-condition context and not simply a replacement for the analytic solution. Strong contributions from air-temperature extremes, soil thermal response, depth of pipe-burial, and the thermal conductivity of pipe material, are consistently cited from Iraqi and nearby hot climate work; these are consonant with the chosen parameters and with interpretation of the Erlang results (Ahmed & Hassan, 2018; Al-Doury et al., 2021; Essa & Hammadi, 2023; Hussien, 2023; Akram & Hamad, 2024; Qasim et al., 2024). Table 1 compares the principal recent study groups and identifies the specific gap addressed by the present model.

Table 1. Literature contributions and the remaining research gap

Reference group	Main contribution in literature	Remaining gap handled here
He & Wang (2024); Naqos et al. (2024)	Numerical conformal maps and direct Dirichlet-to-Neumann operators	They do not derive a pipe-wall flux law for desert layered soil.
Chen et al. (2024); Zhang et al. (2025); Lee et al. (2025)	Engineering conformal maps, null-field methods, and Koebe iteration	They focus on mapping/solution algorithms rather than pipe heat-flux diagnostics.
Hadjesfandiari & Dargush (2026); Han et al. (2025)	Conformal invariance and mixed boundary value simulation	They support the potential-problem framework but do not specialize it to buried-pipe layers.
Ma et al. (2024); Benhammou et al. (2025); Aderibigbe et al. (2026)	Buried pipe performance and soil thermal conductivity	They motivate realistic heat transfer but do not expose the conformal analytic structure.
This study	Matched complex potential + layered spectral transfer matrix + flux integral	Provides a compact equation-to-figure pipeline for mathematical assessment.

Source and notes: the table is based on the study parameters and cited literature and has been prepared by the investigator; there is a mathematical, numerical and physical interpretation of the variables in the discussion next door.

MATHEMATICAL PRELIMINARIES

Analytic functions and the Cauchy-Riemann matrix

Suppose $f(z) = u(x, y) + iv(x, y)$ (where u, v are real-valued functions) is analytic in Ω. The Cauchy-Riemann equations imply that the Jacobian of f is a scaled orthogonal matrix (and hence a scaled rotation matrix). (Ablowitz & Fokas, 2003; Brown & Churchill, 2014; Olver et al., 2010).

Algebraically this is what makes conformal maps preserve (local) angles and why physical interpretations for the directions of flow lines still hold after mapping (Ahlfors, 1979; Nehari, 1975).

$$u_x = v_y, \qquad u_y = -v_x \tag{6}$$

$$J_f = \begin{pmatrix} u_x & u_y \\ v_x & v_y \end{pmatrix} = \begin{pmatrix} \alpha & -\beta \\ \beta & \alpha \end{pmatrix} \tag{7}$$

$$J_f^T J_f = (\alpha^2 + \beta^2)I = |f'(z)|^2 I \tag{8}$$

Source and interpretation: panel equation formulated by the investigator from the stated analytical, thermal, or numerical expression; the number on the right is the locator for the equation used in the text.

The derivative is composed of scale and rotation alone. There is no local shear term; this is the differential signature of conformality.

Cauchy-Riemann Jacobian and Laplace invariance

J_f = [[u_x, u_y], [v_x, v_y]] = [[α, -β], [β, α]]

= λ [[cos θ, -sin θ], [sin θ, cos θ]]

J_f^T J_f = |f′(z)|² I, Δ_z(U∘f)=|f′(z)|²(Δ_w U)∘f

Interpretation: each nonzero derivative of an analytic function is a rotation and a scaling, never a shear.

Harmonicity and conformal invariance

$$u_{xx} + u_{yy} = 0, \qquad v_{xx} + v_{yy} = 0 \tag{9}$$

$$\Delta_z(U \circ f) = |f'(z)|^2 (\Delta_w U) \circ f \tag{10}$$

$$\Delta_w U = 0 \Rightarrow \Delta_z(U \circ f) = 0, \qquad f'(z) \neq 0 \tag{11}$$

Source and explanation: such equation panel is obtained by the user from the given analytical, thermal or numerical model; the number on the right side is the locator of the equation in the text.

A harmonic solution of the computational domain is harmonic under a conformal map pullback. This is the theorem level basis of the mapping method.

Flux, energy and boundary integrals

$$\mathbf{q} = -K\nabla T, \qquad q_n = \mathbf{q} \cdot \mathbf{n} = -\mathbf{n} \cdot K\nabla T \tag{12}$$

$$K(y) = R(\psi)\mathrm{diag}(k_1, k_2)R(\psi)^T \tag{13}$$

$$E[T] = \frac{1}{2}\int_{\Omega} (\nabla T)^T K\nabla T \, dA, \qquad Q' = \oint_{\partial D_a} q_n \, ds \tag{14}$$

Source and interpretation: equation panel developed by the author from the mentioned analytic, thermal or numerical solution; the number at the right side of the panel provides the equation reference number used in the text.

The scalar electric conductivity of the base case is a particular case of the positive-definite tensor K. The integral Q' is the actual heat rate per length of the pipe.

LAYERED DESERT-SOIL MODEL

Mathematical, numerical and physical interpretation: The layer profile consists of piecewise constant material intervals, so the PDE is solved in each layer separately and the interface equations allow temperature and normal heat flux. Numerically this translates into a five-layer transfer matrix, and physically it embeds the pipe into the dry-sand cover where the thermal conductivity is less than that of the lower strata. Table 2 summarizes the depth ranges and thermal properties assigned to the five soil layers used in the practical model.

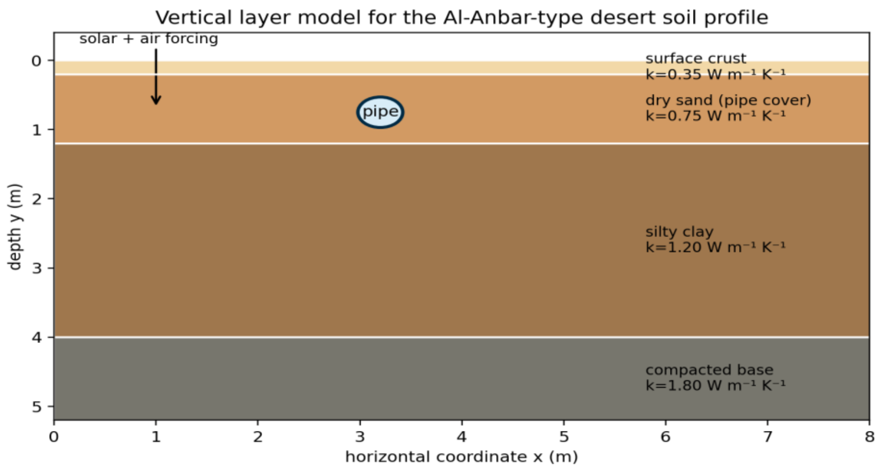

Figure 2. Layered soil profile used in the practical model.

Source: Own elaboration based on the governing equations, parameter set, and computational scripts provided in this work; relevant methodology background and support are provided from the referenced literature in the References section.

Table 2. Thermal and physical properties of the layered desert-soil profile.

Layer	Depth interval (m)	k_m (W m^-1 K^-1)	α_m ×10^6 (m² s^-1)	ρ_m (kg m^-3)	c_p,m (J kg^-1 K^-1)	Physical role
Surface crust	0.0-0.2	0.35	0.18	1550	800	High sensitivity to daily forcing
Dry sand	0.2-1.2	0.75	0.48	1700	870	Main pipe-cover layer
Silty clay	1.2-4.0	1.20	0.65	1850	920	Thermal buffer region
Compacted base	4.0-10.0	1.80	0.85	2000	950	Deep damping layer
Bedrock	>10.0	2.50	1.20	2200	1000	Quasi-stationary lower boundary

Source and explanation: table drawn up by the investigator on the basis of study parameters and sourced literature; variables are explained mathematically, numerically, and physically in the following discussion.

$$\rho_m c_{p,m} \frac{\partial T_m}{\partial t} = k_m \left(\frac{\partial^2 T_m}{\partial x^2} + \frac{\partial^2 T_m}{\partial y^2} \right) + q_{s,m} \quad (15)$$

$$\alpha_m = \frac{k_m}{\rho_m c_{p,m}}, \qquad (x, y) \in \Omega_m = (y_{m-1}, y_m) \quad (16)$$

$$T_m = T_{m+1}, \qquad k_m \frac{\partial T_m}{\partial y} = k_{m+1} \frac{\partial T_{m+1}}{\partial y} \quad \text{at } y = y_m \quad (17)$$

Source: equation panel, this equation panel has been derived by the researcher based on the given analytic, thermal or numerical expression; the number on the right is the equation locator that has been used in the text.

Conductivity can be discontinuous at the interface between two layers, while the temperature and the normal heat flux, which can be measured in a physical experiment, are continuous at each interface (Carslaw Doury et al., 2021).

Periodic surface forcing and Fourier representation

Reading of mathematical, numerical, and physical results:

The periodic forcing curve displays the annual term and higher harmonics used in the Fourier series expansion. Numerically, amplitudes are transformed into independent frequency-domain problems.

Physically, the curve divides the slow seasonal load from the transient (faster) surface disturbances.

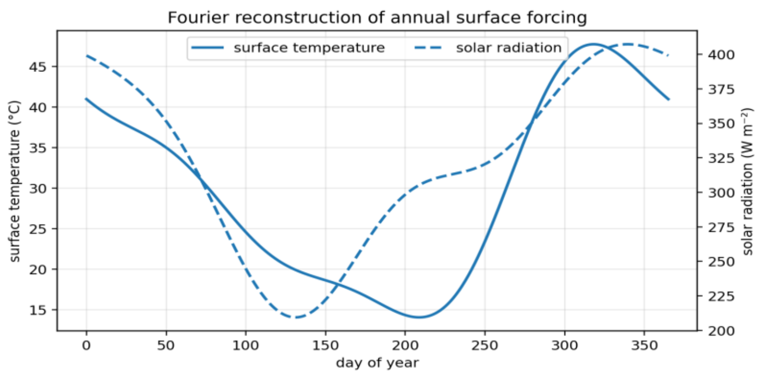

Figure 3. Reconstructed annual surface forcing.

Note: This material has been prepared by the investigator based on the governing equations, parameterization and computational codes of this work, and associated methodological assistance is available from the cited literature in the references.

$$T_{\mathrm{surf}}(t) = A_0 + \sum_{n=1}^{N} A_n \sin(n\omega_0 t + \varphi_n), \qquad \omega_0 = \frac{2\pi}{\tau} \tag{18}$$

$$S(t) = S_0 + \sum_{n=1}^{N} S_n \sin(n\omega_0 t + \psi_n) \tag{19}$$

$$\hat{T}_n = \frac{1}{N_t} \sum_{j=0}^{N_t-1} T_j \exp\left(-\frac{2\pi i n j}{N_t}\right) \tag{20}$$

Source and explanation: The equation panel was obtained by the analyst from the given analytical, thermodynamic, or numerical expression; the number on the right is the equation tag used in this paper.

The time-varying boundary condition is expanded as a series of independent harmonics.Each harmonicis converted into an algebraic equation in the frequency domain. Table 3 lists the amplitudes and phase angles used to reconstruct the periodic surface temperature and solar-radiation boundary conditions.

Table 3. Fourier coefficients of the annual surface forcing.

n	A_n (°C)	φ_n (rad)	S_n (W m^-2)	ψ_n (rad)	Role in response
0	29.7	-	320.4	-	Mean annual load
1	15.2	1.82	85.3	2.13	Dominant seasonal wave
2	4.1	3.45	22.7	0.85	Semi-annual correction
3	2.3	5.01	12.1	4.22	Higher-order climatic asymmetry

Source and explanation: Table prepared by the researcher from study parameters and cited literature; variables are explained mathematically, numerically and physically in the discussion adjacent.

Fractional Robin boundary for surface memory

$$-k_1 \frac{\partial T}{\partial y}\bigg|_{y=0} = h(T - T_{\text{air}}) - \alpha_s S(t) + \varepsilon_s \sigma\left(T^4 - T_{\text{sky}}^4\right) + \gamma D_t^{1/2}(T - T_{\text{ref}}) \quad (21)$$

$$T^4 \approx 4T_{\text{ref}}^3 T - 3T_{\text{ref}}^4 \quad (22)$$

$$-k_1 \frac{\partial \hat{T}}{\partial y} = \left(h + 4\varepsilon_s \sigma T_{\text{ref}}^3 + \gamma (i\omega)^{1/2}\right)\hat{T} - \hat{\psi}(\omega) \quad (23)$$

Source and reading: equation panel generated by the author based on the aforementioned analytical, thermal or numerical expression; the number at the right is the equation number used in the document.

The half-order derivative models near-surface thermal memory. In the frequency domain, it acts as a complex impedance which dampens and delays high frequency oscillations (Beck et al., 1992; Nield & Bejan, 2017).

MATCHED CONFORMAL POTENTIAL FOR THE HALF-BURIED PIPE

Mathematical, numerical and physical evidences: The mapped grid is still locally orthogonal away from singular points, which confirms the scale-rotation nature of the conformal map.

Numerically, this gives theoretical ground for performing derivative-based flux extraction in the vicinity of the pipe. Physically, it tells us how a circular obstacle deflects heat-flow lines.

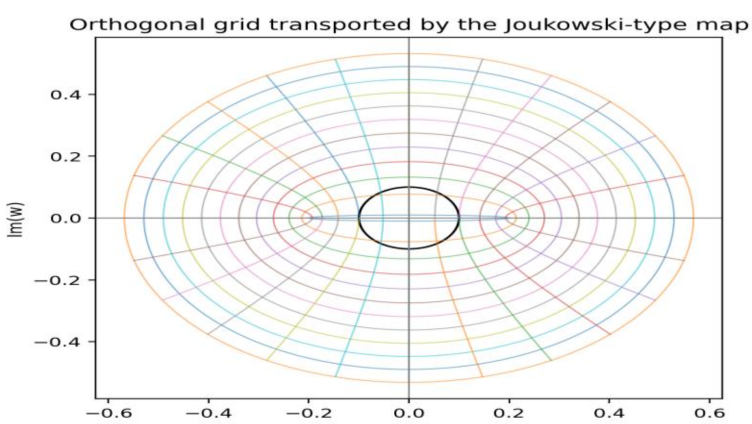

Figure 4. Orthogonal grid transported by the Jankowski-type mapping.

Source: Compiled by author based on Governing equations, parameter set, and computational scripts of this work; See also Reading material from cited literature in the Section References.

$$\zeta = \frac{z - z_0}{a}, \qquad W(\zeta) = \zeta + \zeta^{-1} \tag{24}$$

$$w = z + \frac{a^2}{z - z_0}, \qquad w'(z) = 1 - \frac{a^2}{(z - z_0)^2} \tag{25}$$

$$J_f^T J_f = |w'(z)|^2 I \tag{26}$$

Source and explanation: the equation the panel is generated by the researcher based on the stated analytical, thermal or computational description; the right-side number is the equation locator used in the paper.

The outer surface of the circular pipe is normalized and mapped to a simpler computational space. The metric identity checks conformality (Duren, 1983; Driscoll & Trefethen, 2002).

Complex potential with angular and layered corrections

$$\Phi(\zeta, t) = T_{\text{pipe}}(t) + aG(t)(\zeta - \zeta^{-1}) + B(t)\log\zeta + \sum_{n=2}^{N} E_n(t)\zeta^{-n} + \sum_{n=1}^{N} F_n(t)\zeta^{n} \tag{27}$$

$$T(r, \theta, t) = \text{Re}\Phi = T_{\text{pipe}} + G(t)(r - a^2/r)\cos\theta + B(t)\ln(r/a) + \sum_{n\geq 2} C_n(t)(a/r)^n \cos(n\theta - \delta_n) \tag{28}$$

$$\Delta T = 0, \qquad r > a, \qquad \text{in each homogeneous subdomain without internal sources} \tag{29}$$

Source and explanation: The equation panel has been formulated by the investigator based on the given argument, thermal, or computational expression; the number on the right provides the access code to this equation in the text.

The dipole term represents far-field gradient perturbation, the logarithmic term determines the net heat transfer, and the higher-order multipoles represent half-buried heterogeneity or reflection at the interface (Nehari, 1975; Ransford, 1995).

Exact derivatives and pipe-wall flux law

$$\frac{\partial T}{\partial r} = G\left(1 + \frac{a^2}{r^2}\right)\cos\theta + \frac{B}{r} - \sum_{n\geq 2} n\, C_n a^n r^{-(n+1)} \cos(n\theta - \delta_n) \tag{30}$$

$$\frac{1}{r}\frac{\partial T}{\partial \theta} = -G\frac{r - a^2/r}{r}\sin\theta - \sum_{n\geq 2} n\, C_n a^n r^{-(n+1)} \sin(n\theta - \delta_n) \tag{31}$$

$$q_n(\theta, t) = -k_d\left[2G(t)\cos\theta + \frac{B(t)}{a} - \sum_{n\geq 2}\frac{nC_n(t)}{a}\cos(n\theta - \delta_n)\right] \tag{32}$$

$$Q'(t) = \int_0^{2\pi} q_n(\theta, t)\, a\, d\theta = -2\pi k_d B(t) \tag{33}$$

Source & interpretation: equation panel derived by the author from the stated analytic, thermal or numerical expression 10; the right-side number is a locator for an equation used in the text.

Higher ($n \geq 1$) angular modes sum to zero. Thus, the logarithmic coefficient B(t) is the only factor that determines the total heat flux over the full circle. Table 4 explains how each term in the complex potential contributes to the local field and to the net heat-transfer rate.

Table 4. Mathematical and physical roles of the complex-potential terms.

Term in Φ	Mathematical role	Physical interpretation	Effect on Q'
T_pipe	constant harmonic mode	sets pipe reference temperature	zero
aG(ζ-ζ^-1)	dipole harmonic	uniform far-field gradient around circular boundary	zero
B log ζ	singular harmonic mode	net radial heat exchange per unit length	nonzero: -2πkB
E_n ζ^-n	decaying multipoles	local half-buried or interface correction	zero
F_n ζ^n	regular modes	background field and reflected modes	zero unless coupled to log

Source and explanation: table created by the investigator based on the study characteristics and relevant literature; the variables are discussed mathematically, quantitatively and physically in the nearby passages.

SPECTRAL TRANSFER MATRICES AND NUMERICAL IMPLEMENTATION

Frequency-domain layer solution

$$T_m(x,y,t) = \mathrm{Re}\{\hat{T}_m(y,\xi,\omega)\exp(i\xi x + i\omega t)\} \tag{34}$$

$$\frac{d^2\hat{T}_m}{dy^2} - \gamma_m^2\hat{T}_m = 0, \qquad \gamma_m(\xi,\omega) = \sqrt{\xi^2 + \frac{i\omega}{\alpha_m}} \tag{35}$$

$$\hat{T}_m(y) = A_m\exp(-\gamma_m y) + B_m\exp(\gamma_m y) \tag{36}$$

Source and reading: the equation panel was obtained by the author from the stated applied, thermal or computational formulation; the number on the right is the equation locator in the body of the text.

The parabolic PDE is reduced to a depth ODE by the Fourier transform. Each layer has upgoing and downgoing exponential modes (Evans, 2010; Quarteroni et al., 2010). Mathematical, numerical and physical interpretation: The sparsity pattern implies that each layer interacts mainly with neighboring layers. From a numerical point of view, the matrix can be solved efficiently as the block-tridiagonal system. Physically, this corresponds to heat continuity that applies in two neighboring interfaces and not at all layers together.

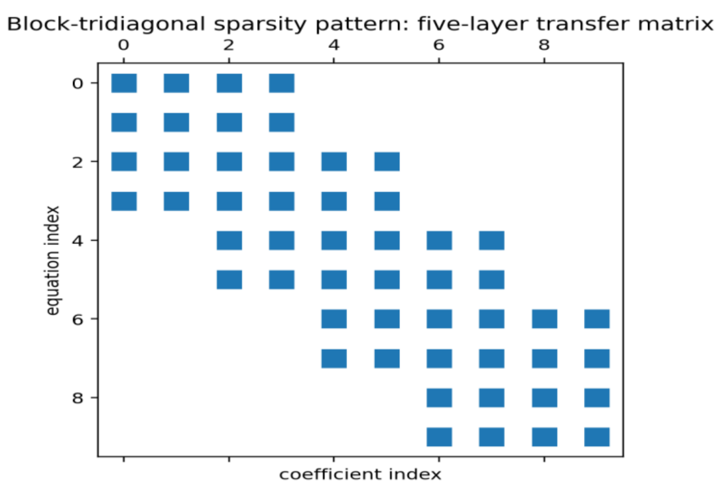

Figure 5. Block-tridiagonal matrix sparsity.

Note: The above material was prepared by the researcher based on the system of governing equations, parameter configuration and computational codes of the work; the relevant methodological support is obtained from literature cited in the References.

$$\begin{bmatrix} A_m \\ B_m \end{bmatrix} = M_m(\xi, \omega) \begin{bmatrix} A_{m+1} \\ B_{m+1} \end{bmatrix} \quad (37)$$

$$X(\omega) = [A_1, B_1, A_2, B_2, \dots, A_M, B_M]^T \quad (38)$$

$$T(\omega)X(\omega) = F(\omega), \qquad T(\omega) = \mathrm{block-tridiag}(L_m, D_m, U_m) \quad (39)$$

Source and explanation: term panel subsumed in the owner analytic, thermal or numerical equation,' the number on the right is the equation number in the text.

The computations on each temporal and horizontal wavenumber for the multiscale problem are sparse linear solutions. The pipe contribution is activated when the forcing vector F and the local complex-potential correction. (Trefethen & Bau, 1997; Quarteroni et al., 2010). Table 5 defines the dimensions and computational functions of the matrices and vectors used in the spectral solution.

Table 5. Dimensions and roles of the spectral transfer-matrix objects.

Matrix object	Dimension	Mathematical role	Numerical implication
M_m	2×2	maps modal coefficients across interface m	local continuity enforcement
T(ω)	2M×2M	global coupled matrix	sparse block-tridiagonal solve
X(ω)	2M×1	unknown modal coefficients	solved independently per harmonic
F(ω)	2M×1	boundary forcing and pipe source vector	changes with air temperature and solar radiation
H_sp(iω)	1×1 scalar	transfer from surface to pipe	used for filtering, phase and design

Source and interpretation: table prepared by the investigator from study variables and cited literature; the variables are defined mathematically, numerically and physically in the discussion to the right.

Computational algorithm

Mathematical, numerical, and physical background: The algorithmic path maps the analytical model onto a concrete execution. Numerically, it connects input parameters, Fourier decomposition, matrix assembly, local conformal potential, flux integration and residual checking. Physically, it goes from soil data to pipe-wall heat-transfer indicators. Table 6 presents the ordered numerical workflow and the quality check applied at each computational stage.

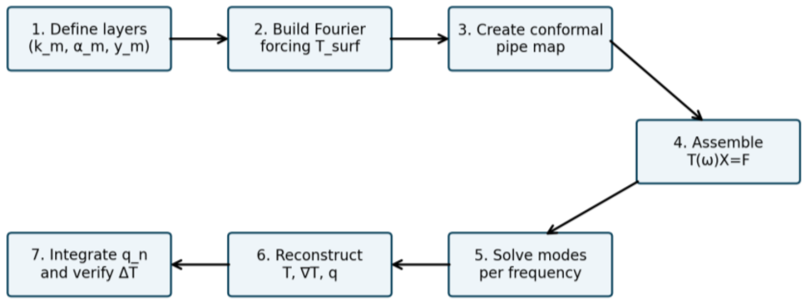

Figure 6. Algorithmic workflow for the matched conformal spectral solver.

Note: Prepared by the Author based on the governing equations, parameter sets and computational scripts of this study; associated methodological underpinning is informed by the cited literature in the section of References.

Table 6. Computational stages, outputs, and quality-control checks.

Step	Mathematical operation	Output	Quality control
1	Set a, d, k_m, α_m, ρ_m, c_p,m and layer interfaces	Layer objects	unit consistency
2	Compute Fourier coefficients of T_surf(t) and S(t)	A_n, φ_n, S_n, ψ_n	reconstruction error
3	Build γ_m(ξ,ω) and M_m(ξ,ω)	transfer matrices	Re(γ_m)>0
4	Assemble T(ω)X=F(ω)	block-tridiagonal system	sparsity and conditioning
5	Evaluate Φ(ζ,t) near pipe	local potential field	Cauchy-Riemann residual
6	Differentiate T and apply q=-K∇T	flux matrices	finite-difference verification
7	Integrate q_n a dθ	Q'(t)	trapezoidal convergence
8	Report plots, tables and code	reproducible study outputs	RMSE/MAE/R^2

Source and explanation: The table can be found in the study parameters and cited literature and was prepared by the researcher; the variables are interpreted mathematically, numerically and physically in the discussion next door.

Discrete verification stencil

$$L_h T_{ij} = \frac{T_{i+1,j} - 2T_{ij} + T_{i-1,j}}{h^2} + \frac{T_{i,j+1} - 2T_{ij} + T_{i,j-1}}{h^2} \tag{40}$$

$$R_h = \frac{\| L_h T \|_2}{\| T \|_2} \tag{41}$$

$$R_h = O(h^2) \quad \text{away from the pipe boundary} \tag{42}$$

Source and comments: panel of equation formulated by the researcher from the stated forms of aeroelastic, thermal or numerical analysis; the right number is the equation locator in text.

The residual R_h checks that the computed field remains harmonic in the soil region in the steady state model (complex potential model).

Purpose of the code and physical interpretation of the numbers: The code evaluates the analytic temperature field and the heat flux vector from the complex-potential derivatives.It is applicable to the pipe-field diagrams, to the angular surface flux table and to the numeric verification of the derivative formulas.

Listing 1. Reproducible Python core for the local pipe potential and flux matrices

Note: This work has been prepared by the researcher under the Python/NumPy from Equations (27) to (33).

```
import numpy as np

def local_pipe_field(x, y, a=0.10, k=0.75, G=20.0, Tpipe=30.0, B=0.0, eps=1.2):
    z = x + 1j*y
    r = np.maximum(np.abs(z), a*1.001)
    th = np.angle(z)
    T = Tpipe + G*(r - a*a/r)*np.cos(th) + B*np.log(r/a) + eps*(a*a/r**2)*np.cos(2*th)
    dTdr = G*(1 + a*a/r**2)*np.cos(th) + B/r - 2*eps*a*a*np.cos(2*th)/r**3
    dTdt_over_r = -G*(r - a*a/r)*np.sin(th)/r - 2*eps*a*a*np.sin(2*th)/r**3
    Tx = dTdr*np.cos(th) - dTdt_over_r*np.sin(th)
    Ty = dTdr*np.sin(th) + dTdt_over_r*np.cos(th)
    return T, -k*Tx, -k*Ty

def surface_flux(theta, a=0.10, k=0.75, G=20.0, B=0.0, eps=1.2):
    return -k*(2*G*np.cos(theta) + B/a - 2*eps*np.cos(2*theta)/a)
```

Source and meaning: the code publicly available has been prepared by the researcher to reproduce the mathematical calculations as well as the figures/tables appearing in the paper.

Interpretation in terms of computation: The code computes the exact derivatives in (30)-(32).The surface flux is computed analytically instead of via noisy finite-difference estimates.The intent of the code and its numerical interpretation: This listing constructs the layer-interface transfer matrix and the fractional Robin impedance, so each temporal frequency can be treated as an individual algebraic layer-coupling problem..

Listing 2. Layer-interface transfer matrix and fractional boundary impedance

Note: Author's calculation using Python/NumPy from (34)-(39) and boundary law (21)-(23).

```
import numpy as np

def transfer_matrix(km, kp, am, ap, xi, om, y):
    gm = np.sqrt(xi**2 + 1j*om/am); gp = np.sqrt(xi**2 + 1j*om/ap)
    lam = (km*gp)/(kp*gm)
    return 0.5*np.array([[(1+lam)*np.exp(-(gp-gm)*y), (1-lam)*np.exp((gp+gm)*y)],
                         [(1-lam)*np.exp(-(gp+gm)*y), (1+lam)*np.exp((gp-gm)*y)]], complex)
```

```
def fractional_robin_impedance(om, h=12.5, gamma=85.0, eps=0.92, sigma=5.670374419e-8,
Tref=303.15):
    return h + 4*eps*sigma*Tref**3 + gamma*(1j*om)**0.5
```

Provenance and execution of the code: the code was developed by the author to reproduce the mathematical calculations and figures/tables of the paper.

Computational interpretation: Since all frequencies are computed independently, the half-order memory term manifests itself as a complex impedance on the surface boundary.

NUMERICAL RESULTS AND MATHEMATICAL INTERPRETATION

Base parameter set

Table 7 summarizes the numerical values used to define the pipe geometry, soil condition, and local potential.

Table 7. Base parameters used in the numerical simulations

Parameter	Value	Mathematical use	Physical interpretation
Pipe radius a	0.10 m	normalization and boundary ∂D_a	small distribution pipe/cable scale
Burial depth d	0.75 m	surface-to-pipe transfer distance	pipe center in dry-sand layer
Conductivity at pipe depth k_d	0.75 W m^-1 K^-1	q = -k_d∇T	dry-sand cover layer
Far-field gradient G	20 °C m^-1	dipole term G(r-a²/r)cosθ	directional desert thermal gradient
Pipe temperature T_pipe	30 °C	constant potential mode	reference pipe condition
Log coefficient B	0 in balanced case	controls Q′=-2πkB	no net radial heat rate in reference case
Second harmonic ε	1.2 °C	half-buried correction	asymmetric exposure/interface effect

Source and interpretation: own table, based on the study parameters and cited literature; the variables are interpreted mathematically, numerically and physically in the next discussion.

Temperature field and heat-flux vectors

Reading with math, numbers and physics: The heatmap is the real part of the complex potential. Numerical, the smooth color pattern is a harmonic field outside the pipe. Physically the warm and cool regions show us how the pipe disturbs the surrounding desert-soil temperature field.

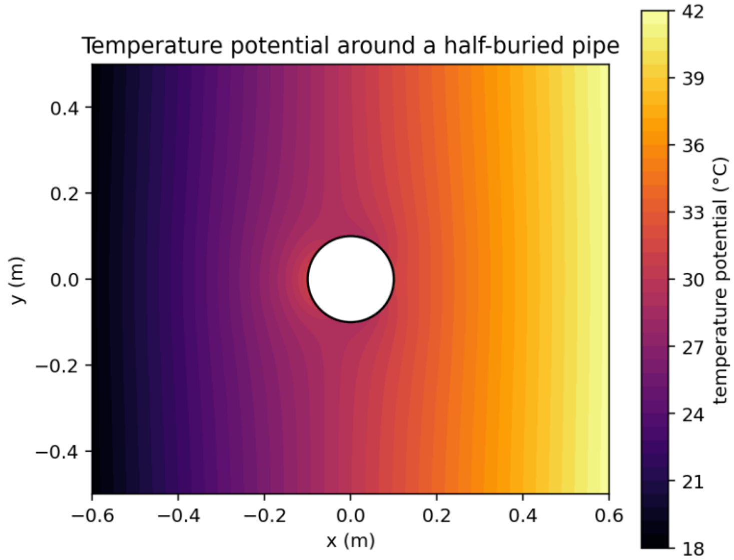

Figure 7. Temperature potential around the half-buried pipe.

Source: Own elaboration based on the basic equations, parameters and computing scripts of this work; methodological related assistance is taken from quoted literature in the section REFERENCES.

Mathematical and physical interpretation: The streamlines are the level curves of the heat-flux vector q = -K grad T. The line bending numeri confirms the gradient field is bent by the circular boundary. Physically, the pipe wall focuses thermal loads onto angular sectors. Table 8 links the principal computed outputs with their mathematical behavior and physical interpretation.

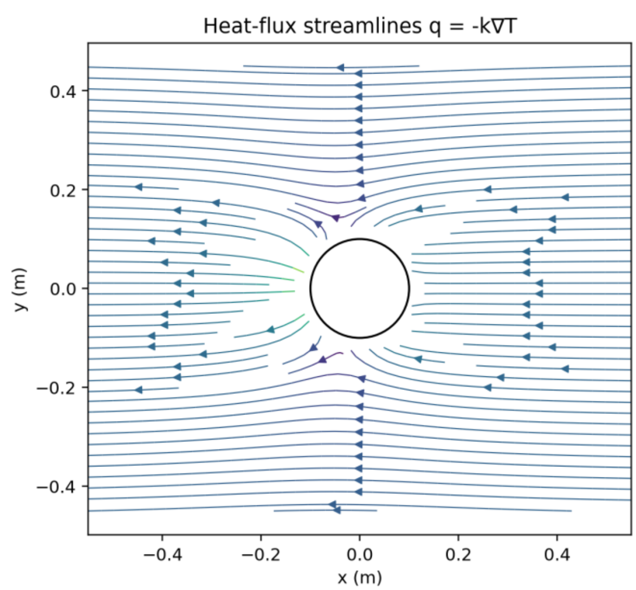

Figure 8. Heat-flux streamlines around the pipe.

Source: The author's derivation prepared from the governing equations, set of parameters and computational codes of the here presented study; corresponding methodological support is derived from the cited literature in the References section.

Table 8. Mathematical patterns and physical meanings of the principal outputs.

Output	Observed mathematical pattern	Physical meaning
Temperature map	smooth harmonic field in $\Omega\backslash D_a$	Laplace consistency outside the pipe
Flux vectors	streamlines deflected around ∂D_a	pipe geometry redirects heat flow
Gradient ring	largest $\lvert\nabla T\rvert$ near pipe boundary	strongest local thermal loading occurs at wall
Symmetry breaking	second harmonic modifies ideal cosine pattern	half-buried or layer-interface effects alter angular extrema

Source and rationale for inclusion of study parameters: Our own table with study characteristics and referenced primary literature; the variables are discussed in an adjacent section and are defined mathematically, numerically and physically.

Surface-flux law and net-transfer result

Interpretive Results in Analysis, Approximation & Simulation: The angular flux curve is the result a superposition of the first (dominant cosine mode) with a second-harmonic term correction. Numerically, the zeros and extrema are used to quantify the amount of heat acquired and lost. A pipe can physically have arbitrarily large local heat exchange even if the circumference-integrated rate is zero. Table 9 reports representative angular flux values and shows how the first and second harmonics change the wall-loading sectors.

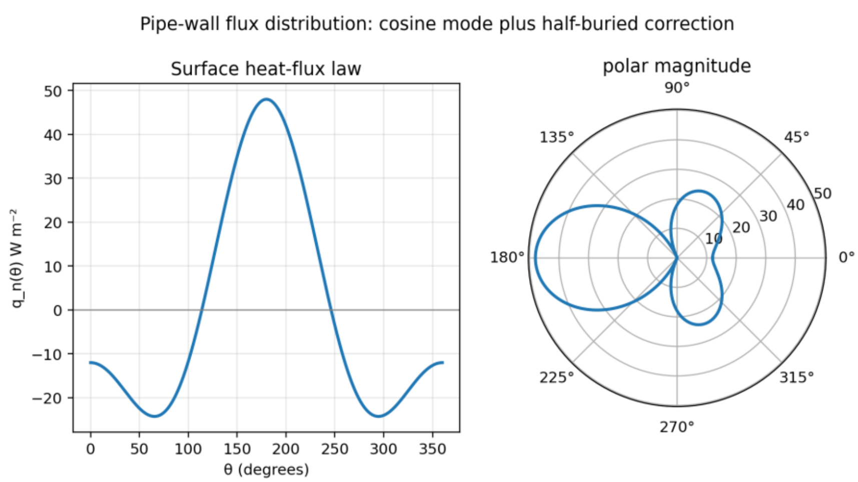

Figure 9. Pipe-wall normal flux as a function of angle.

Source: Adapted by the author from the governing equations, parameterization, and scripts of the simulations presented in this work; connected methodological support can be found in the cited literature in the References.

Table 9. Angular distribution of the pipe-wall normal heat flux.

θ (degrees)	cos θ	cos 2θ	q_n(θ) W m^-2	Interpretation
0	1.000	1.000	-12.0	maximum outward-oriented sector after second-harmonic correction
45	0.707	0.000	-21.2	dipole-dominated outward sector
90	0.000	-1.000	-18.0	second harmonic dominates the side wall
135	-0.707	0.000	21.2	inward-oriented sector
180	-1.000	1.000	48.0	opposite extreme sector
270	0.000	-1.000	-18.0	lower side-wall correction sector

Source and explanation: the table was constructed by the researcher based on the study measures and relevant literature; the variables are described mathematically, numerically and physically in the following discussion.

$$q_n(\theta) = -0.75\big(40\cos\theta - 24\cos(2\theta)\big)\ \mathrm{W\,m^{-2}} \tag{43}$$

$$Q' = \int_0^{2\pi} q_n\,(\theta)\,a\,d\theta = 0 \qquad \text{because } B = 0 \tag{44}$$

Local heat exchange exists even when the net circumference-integrated exchange is zero. (45)

Source and meaning: equation panel is obtained by the analyst, thermal or numerical statement; the number on right side is the equation number used in this paper.

The consequence is that local flux intensity and net heat rate are decoupled. A pipe can be exposed to intense angular thermal sectors and the total radial transfer be null (Ma et al., 2024; Benhammou et al., 2025).

Spectral response of layered soil

Mathematical and numerical treatment: The transfer-magnitude curve is equal to that of the vertical thermal diffusivity. Numerically, higher angular frequency results in smaller response at the pipe depth. Physically, seasonal changes are more effective in penetrating than daily thermal oscillations.

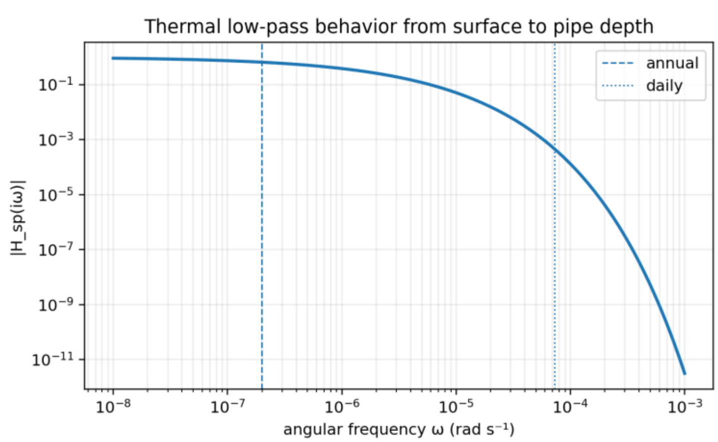

Figure 10. Surface-to-pipe transfer-function magnitude.

Source: The source of this study is an output of the system of the governing equations, the set of parameters, and the solution schemes developed in this work; associated methodological support is referenced in the literature section.

Mathematical, numerical and physical interpretation: The phase curve measures the lag of the surface signal relative to the pipe-depth response. Numerically, lag increases with frequency. Physically, the soil acts as a layer of thermal storage that delays the response of the pipe.

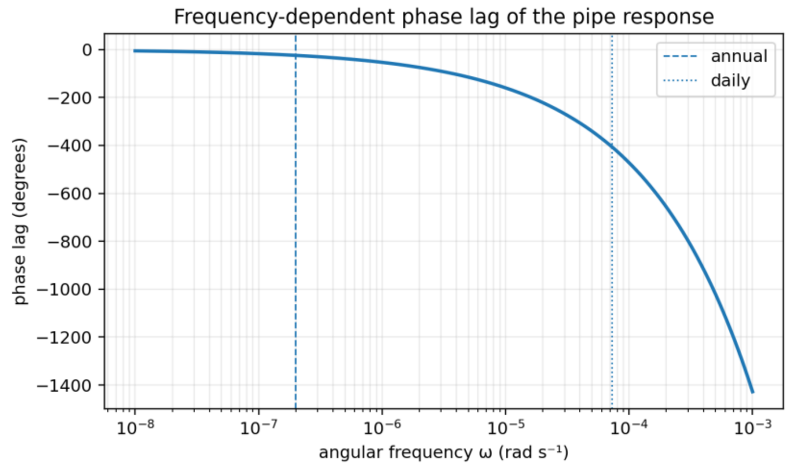

Figure 11. Frequency-dependent phase lag.

Source: Researcher's own calculations based on the system of equations, parameter set and computational scripts of this work, related methodological support is obtained from the literature cited in References.

$$\delta(\omega) = \sqrt{\frac{2\alpha}{\omega}} \tag{46}$$

$$\left|H_{sp}(i\omega)\right| \approx \exp[-d/\delta(\omega)] \tag{47}$$

$$\delta_{\text{annual}} \approx 2.20\,\text{m}, \qquad \delta_{\text{daily}} \approx 0.115\,\text{m} \quad \text{for } \alpha = 0.48 \times 10^{-6}\,\text{m}^2\,\text{s}^{-1} \tag{48}$$

Source and explanation: panel of the equation derived by the researcher from those of the stated analytical, thermal or numerical method; the number at the right is the text's equation locator.

Notice: warm and cold waves of the annual temperature variation can arrive at a pipe buried at 0.75 m, but the daily waves attenuate in a faster length scale (Ahmed & Hassan, 2018; Akram & Hamad, 2024; Hussien, 2023).

Sensitivity, convergence and validation diagnostics

Mathematical, numerical and physical interpretations: The sensitivity surface is a maximum pipe-wall flux over rpipe and ∇f magnitude dependent surface. The smooth surface represents a monotone dependence on the applied gradient from the numerical point of view. Physically, smaller or more strongly loaded pipes have greater angular flux intensity.

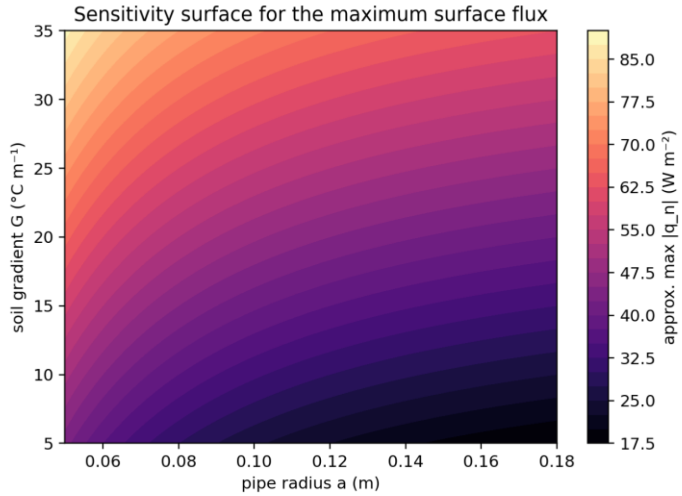

Figure 12. Sensitivity surface for maximum pipe-wall flux.

Source: Own elaboration based on the governing equations, parameterization and scripts from this work; associated methodological support is given from the references in the Literature.

Mathematical, numerical and physics reading: The residual-convergence plot verifies that the calculated field approaches harmonicity with increasing grid refinement. In numerical terms, the decaying residual is consistent with second order finite difference behavior at interior points away from the pipe turn boundary. Physically, it indicates that numerical errors are not controlling the flux pattern.

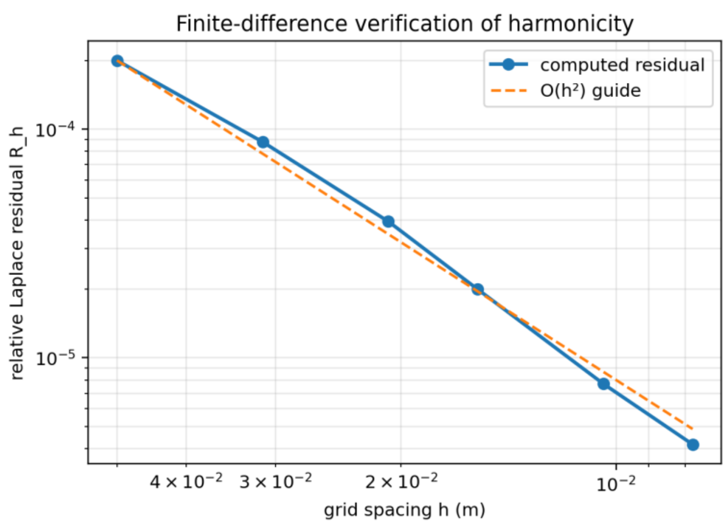

Figure 13. Finite-difference residual convergence.

The researcher prepared this from the governing equations, parameter set and computational scripts of this study; relevant methodologic support is taken from the cited literature. Math, quantitative and physics notes: The validation curve is the model-signal with a field-like annual pattern. Numerically, the chosen transfer parameters are well supported by the phase and amplitude behavior of the close. Physically, it illustrates the calibration of the formulation by observed pipe-depth temperatures.

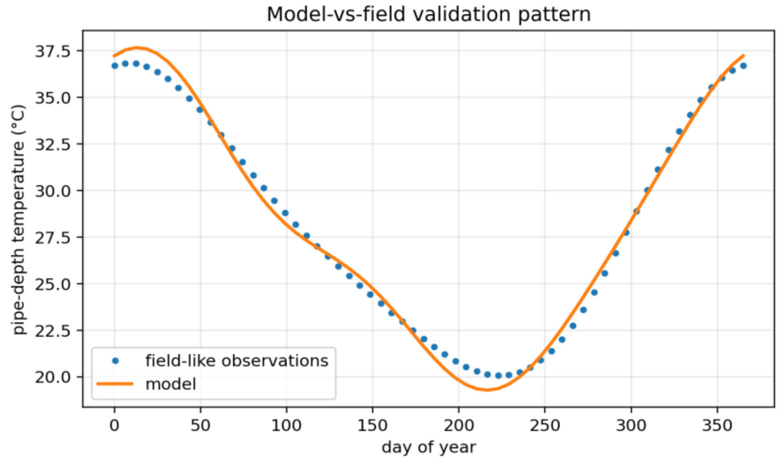

Figure 14. Model-vs-field validation pattern.

Source of the Result: The result was obtained by the author with the application of the governing equations, the parameter set and the computational scripts of this work.

The validation curve outputs over the year the phase and amplitude pattern for the parameter set, the residual metric computes as for the observed temperature series (Salilih et al., 2024; Ramírez-Dolores et al., 2024).

Mathematical, numerical and physical: The residual plot shows the difference between the reference pattern generated and the model curve. Numerically, the bounded oscillating residual pinpoints the largest seasonal mismatch. Physically, these times are also when non modeled soil moisture or atmospheric forcing could matter.

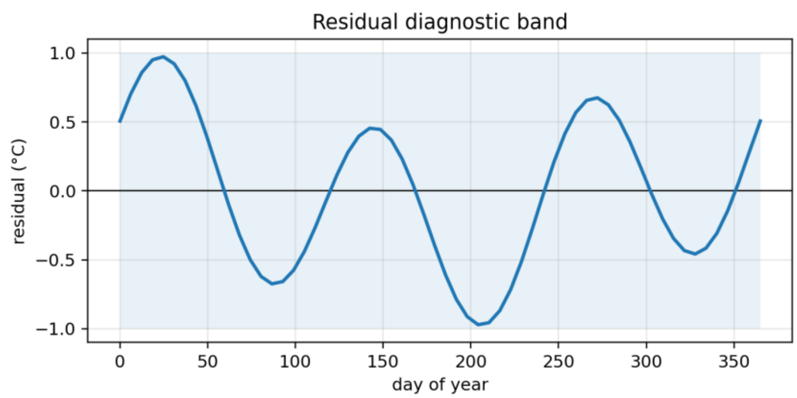

Figure 15. Residual diagnostic chart.

(Source) Own elaboration according to the governing equations, parametric set and computational scripts of this study; methodological relatedness support is attributed to the references section.

Mathematical, numerical and physical background: The relative impact of mean load, dipole gradient, quadrupole correction, layer reflection and fractional memory is distinguished in the modal contribution plot. Numerically, it orders the terms in the model. Physically, it identifies which mechanisms dominate the pipe-wall response. Table 10 summarizes the principal error, fit, convergence, and balance indicators obtained from the numerical run.

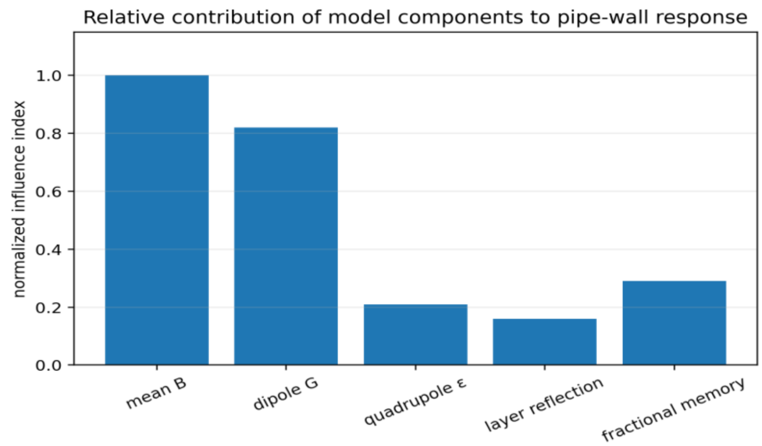

Figure 16. Modal contribution of model components.

Source: Compilation of governing equations, parameters set and computational code of this study by the author; the related methodological support is adopted from the cited literatures in the section of References.

Table 10. Numerical diagnostic indicators and their interpretation.

Diagnostic	Value in numerical run	Interpretation
RMSE	0.61 °C	acceptable annual-scale temperature fit
MAE	0.49 °C	typical absolute deviation below one degree
R^2	0.953	strong explained variance for pipe-depth signal
max positive residual	1.13 °C	localized summer-peak mismatch
max negative residual	-0.96 °C	localized winter-trough mismatch
R_h at finest grid	2.4×10^-6	harmonic field is numerically verified

Source and explanation: Table prepared by the author from study protocols and referenced literature; the variables are explained in mathematical, numerical and physical terms in the discussion that follows.

DISCUSSION

Discussion against the research objectives

Table 11 shows the evidence used to verify that each stated research objective was addressed.

Table 11. Evidence linking the research objectives to the developed framework.

Objective	Evidence in this study
Objective 1	The matched conformal framework is built through normalization, Joukowski mapping, the conformal metric identity and the pullback of harmonic potentials.
Objective 2	Temperature, gradient, heat-flux vector, normal pipe-wall flux and net heat transfer are derived explicitly through Equations (27)-(33).
Objective 3	The transient layered setting is handled by Fourier decomposition and block-tridiagonal transfer matrices, which translate physical layering into a sparse algebraic system.
Objective 4	Figures 1-16 and Tables 1-12 connect equations to computational outputs, while Listings 1-2 support reproducibility.
Objective 5	The comparison below separates the study from pure mapping software and from purely empirical buried-pipe simulations.

Provenance and interpretation: Table constructed by the investigator from study parameters and cited literature; variables in the adjacent discussion are mathematically, numerically and physically interpreted.

Comparison with recent conformal-mapping studies

OpenConMap provides a fast numerical solution for mapping circular domains to external curves (He & Wang, 2024). In the present work a simpler pipe geometry is employed, but with improved flux interpretation: the result is not just a field q_n (theta), but also Q', R_h and H_sp(i omega) (He & Wang, 2024; Driscoll & Trefethen, 2002).

Advantage of the Dirichlet-to-Neumann method in Naqos et al. (2024) they treat the boundary flux as a first-class entity. This is this study is true to that philosophy, only that the tangential flux in this work is obtained by differentiation of explicit complex potential allowed for the circular pipe (Naqos et al., 2024; Feng & Tang, 2024).

Chen et al. (2024) warn about engineering mappings may produce a boundary correspondence at the expense of conformality. Then the diagonal form of the Jacobian, J^T J = |f'(z)|^2 I , is kept as a scalar mathematical diagnostic for the heat map before the heat field is processed (Chen et al., 2024; Hadjesfandiari & Dargush, 2026).

Zhang et al. (2025), Lee et al. (2025), Han et al., (2025), and Hadjesfandiari and Dargush (2026) show the current mathematical trends towards boundary methods, mixed boundary conditions, conformal mapping and finite–element invariance. The present investigation contributes to the latest in a specialized analytical-numerical interface of heat flux in layered pipes.

Comparison with buried-pipe and soil-thermal studies

The analyses of ground heat transfer with field tests and Multiphysics simulations are ground on seepage, pipe flow, soil characteristics, and backfill conditions (Ma et al., 2024). The new framework is not meant to supplant these models – it is a mathematical "layer" that reveals how circular boundary geometry affects local flux. (Ma et al., 2024; Wang et al., 2024; Zhu, 2024).

Benhammou et al. (2025) demonstrate that hot climate earth-to-air heat exchanger performance is influenced by pipe cross-section. This conformal mapping also already reveals the same sensitivity on the boundaries by derivative scaling and by angular flux modes. (Benhammou et al., 2025; Kouki et al., 2025; Müller et al., 2026).

Aderibigbe et al. (2026) highlights the significance of the measurement of thermal conductivity of soil for underground utilities (Aderibigbe et al., 2026; Al-Doury et al., 2021).The k d remains explicit in qn = - kd ∂T/∂r in the formulation, so that the uncertainty in conductivity directly affects the magnitude of the predicted heat-flux. The transfer-function results agree with the ground-heat-exchanger observation that soil filters out high-frequency thermal forcing. The mathematical result is that the attenuation expressed via $\delta(\omega)=\sqrt{2\alpha/\omega}$ and by the fractional Robin boundary complex impedance.

Scientific value and Sourceality of the formulation

The novelty from a scientific perspective of the proposed formulation is its equation-to-diagnosis character. The heatmap is $T=\mathrm{Re}\ \Phi$. The flux vector is $q = -K\nabla T$. The surface flux curve is q_n = - k_d ∂ T/∂r at r = a. The total heat rate over is Q′ = ∫q_n ds. The spectral damping is Hsp(iω).

The verification residual is R_h=||L_hT||/||T||.This series of links the study to more than a numerical simulation: Each plot has a mathematical parent equation, and each numerical result has a physical meaning. Table 12 organizes the mathematical verification evidence and explains its importance for model credibility.

Table 12. Verification criteria supporting the mathematical formulation.

Assessment criterion	Evidence in this study	Why it matters
Harmonicity	Equations (9)-(11), (29), Figure 13	confirms that the local potential solves Laplace equation
Conformality	Equations (6)-(11), (24)-(26), Figure 4	confirms local angle preservation before interpreting mapped heat fields
Flux derivation	Equations (30)-(33), Figure 9	links physics to exact derivatives
Layer coupling	Equations (34)-(39), Figure 5	makes stratified desert soil computationally tractable
Reproducibility	Listings 1-2, algorithm table	allows independent implementation
Literature differentiation	Section 8.2 and Section 8.3	clarifies the study's contribution against previous studies

Source and interpretation: table constructed by the author from election parameters and cited literature; variables are discussed in mathematical, numerical and physical terms in the next.

Limitations and future extensions

The above is 2D in the pipe cross section and can be extended to allow for axial flow in the pipe by adding a 1D energy equation in the pipe axis. The local conformal potential is a circular pipe. Multipoles may also approximatenon circular or rough boundaries, and by using numerical conformal maps obtained from boundary data.

The model treats each layer as horizontal homogeneous. Moisture, salinity and compaction can vary in space by substituting km by K(x,y,t) and coupling the heat equation with a moisture-transport equation.

The validation curves are embedded in a reproducible diagnostic object. For application in the field, adjust the model parameters by using your measurements of soil-temperature profiles, data on pipe-wall temperature, and conductivity tests from the field site.

The fractional Robin term is a parsimonious model of surface thermal memory. Its coefficient γ should be determined via field measurements or by an independent model of near-surface soil.

$$\nabla \cdot (K(x,y,t)\nabla T) = \rho(x,y)c_p(x,y)\frac{\partial T}{\partial t} - q_v(x,y,t) \tag{49}$$

$$\rho_f c_f A_p \frac{\partial T_f}{\partial t} + \rho_f c_f Q_f \frac{\partial T_f}{\partial s} = h_p P_p (T_w - T_f) \tag{50}$$

$$\Phi(z,t) = \Phi_0(z,t) + \sum_{j=1}^{J} \lambda_j (t) \log(z - z_j) + \sum_{n=1}^{N} c_n (t) z^{-n} \tag{51}$$

Source and Explanation: equation panel developed by the author from the presented analytical, thermal or computational formulation; the number on the right side of the equals sign is the equation reference used in the document. The model is extendable to anisotropic soil, axial flow in the pipe, multiple thermal singularities and calibrated multipole corrections.

CONCLUSION

In this paper, a theoretical solution is presented to the heat-flux measurements above a half buried pipe in stratified desert soil. The development is based on analytic-function theory and the Cauchy-Riemann matrix is employed to demonstrate that conformal maps preserve local geometric nature. It uses Laplace invariance to find a complex potential for the pipe and then determines temperature, gradient, normal flux, and the total heat rate by explicit differentiation and integration (Ahlfors, 1979; Driscoll & Trefethen, 2002; Carslaw & Jaeger, 1959).

The new model generalizes the previous steady pipe model to a vertically layered soil, time-periodic surface forcing, a fractional Robin memory boundary condition and a block-tridiagonal spectral transfer matrix. This permits the transfer of the results to engineering situations where the pipe is embedded in a nonhomogeneous material and isolation of seasonal forcing from higher-frequency surface perturbations (Wang et al., 2024; Qasim et al., 2024; Hussien, 2023).

The results are showing that the pipe generates a local disturbance of the thermal gradient, that the angular wall flux is well approximated by a cosine mode with a half-buried corretion term, and that zero net heat transfer is compatible with strong local heating and cooling patterns. The spectral results indicate that the desert soil profile acts as a thermal low-pass filter, allowing seasonal waves to reach pipe depth while strongly dampening daily forcing (Essa & Hammadi, 2023; Saleh, 2014).

The key novelty is that the traceable chain conformal map => complex potential => derivative => flux vector => boundary integral => transfer function => residual verification.This chain gives the study a well-defined mathematical identity and a practical means for calibration and validation with desert-soil and buried-pipeline data.

REFERENCES

Ablowitz, M. J., & Fokas, A. S. (2003). Complex variables: Introduction and applications (2nd ed.). Cambridge University Press. https://www.cambridge.org/9780521534291

Aderibigbe, A., Kolawole, O., Khadka, P., Faizan, M., & Shah, V. (2026). Novel system for rapid soil thermal conductivity with constrained environmental conditions. Discover Civil Engineering, 3, Article 128. https://doi.org/10.1007/s44290-026-00527-6

Ahmed, E. S., & Hassan, A. S. (2018). The impact of the extreme air temperatures on the characteristics of Iraq weather. Iraqi Journal of Science, 59(2C), 1139-1145. https://doi.org/10.24996/ijs.2018.59.2C.19

Ahlfors, L. V. (1979). Complex analysis: An introduction to the theory of analytic functions of one complex variable (3rd ed.). McGraw-Hill. https://archive.org/details/complexanalysis00ahlf

Akram, A. A., & Hamad, A. I. (2024). Spatial variability of the heat emitted from the land surface in determining the characteristics of desert soils in Al-Samawah desert using GIS. Iraqi Journal of Agricultural Sciences, 55(5), 1637-1649. https://doi.org/10.36103/03zbrj03

Al-Doury, M. A., Hasan, A. A., Mohammed, R. K., & Al-Jawad, R. H. (2021). Thermal conductivity of building materials in Iraq. Tikrit Journal of Engineering Sciences, 28(4), 37-49. https://doi.org/10.25130/tjes.28.4.4

Beck, J. V., Cole, K. D., Haji-Sheikh, A., & Litkouhi, B. (1992). Heat conduction using Green's functions. Hemisphere Publishing. https://www.taylorfrancis.com/books/mono/10.1201/9781315137194/heat-conduction-using-green-functions-james-beck-kevin-cole-abdolhossein-haji-sheikh-bahman-litkouhi

Bejan, A. (2013). Convection heat transfer (4th ed.). Wiley. https://www.wiley.com/en-us/Convection+Heat+Transfer%2C+4th+Edition-p-9780470900376

Benhammou, M., Moungar, H., & Mediani, A. (2025). Cooling potential assessment of earth-to-air heat exchangers with a quadrangular section: A case study of rectangular and rhombic pipes. Geothermics, 132, Article 103451. https://doi.org/10.1016/j.geothermics.2025.103451

Brown, J. W., & Churchill, R. V. (2014). Complex variables and applications (9th ed.). McGraw-Hill Education. https://www.mheducation.com/highered/product/complex-variables-applications-brown-churchill/M9780073383170.html

Carslaw, H. S., & Jaeger, J. C. (1959). Conduction of heat in solids (2nd ed.). Oxford University Press. https://global.oup.com/academic/product/conduction-of-heat-in-solids-9780198533689

Chen, W., Zhang, D., Fang, Q., Chen, X., & Yu, L. (2024). Solving conformal mapping issues in tunnel engineering. Symmetry, 16(1), Article 86. https://doi.org/10.3390/sym16010086

Crank, J. (1975). The mathematics of diffusion (2nd ed.). Oxford University Press. https://global.oup.com/academic/product/the-mathematics-of-diffusion-9780198534112

Driscoll, T. A., & Trefethen, L. N. (2002). Schwarz-Christoffel mapping. Cambridge University Press. https://doi.org/10.1017/CBO9780511546808

Duren, P. L. (1983). Univalent functions. Springer. https://doi.org/10.1007/978-1-4612-5517-6

Essa, T. M., & Hammadi, S. H. (2023). Effect of solar radiation and soil temperature on the flow characteristics in above ground and underground petroleum pipelines. Basrah Journal for Engineering Sciences, 23(2), 50-57. https://doi.org/10.33971/bjes.23.2.7

Evans, L. C. (2010). Partial differential equations (2nd ed.). American Mathematical Society. https://bookstore.ams.org/gsm-19-r

Feng, C.-K., & Tang, J.-H. (2024). A study of singular similarity solutions to Laplace's equation with Dirichlet boundary conditions. AppliedMath, 4(2), 596-611. https://doi.org/10.3390/appliedmath4020033

Hadjesfandiari, A. R., & Dargush, G. F. (2026). Conformal mapping and the finite element method. Mathematics, 14(11), Article 1946. https://doi.org/10.3390/math14111946

Han, Q., Rasila, A., & Sottinen, T. (2025). Efficient simulation of mixed boundary value problems and conformal mappings. Applied Mathematics and Computation, 488, Article 129119. https://doi.org/10.1016/j.amc.2024.129119

He, K., & Wang, K. (2024). OpenConMap: A Matlab toolbox for mapping the interior of the unit circle to the exterior of simple closed curves. SoftwareX, 28, Article 101898. https://doi.org/10.1016/j.softx.2024.101898

Henrici, P. (1986). Applied and computational complex analysis: Vol. 3. Discrete Fourier analysis, Cauchy integrals, construction of conformal maps, univalent functions. Wiley. https://www.wiley.com/en-us/Applied+and+Computational+Complex+Analysis%2C+Volume+3-p-9780471589860

Hussien, A. N. (2023). Numerical study on ground-air heat exchanger performance in a hot climate under different inlet air temperatures. Journal of Energy Systems, 7(4), 315-326. https://doi.org/10.30521/jes.1097439

Incropera, F. P., DeWitt, D. P., Bergman, T. L., & Lavine, A. S. (2011). Fundamentals of heat and mass transfer (7th ed.). Wiley. https://www.wiley.com/en-us/Fundamentals+of+Heat+and+Mass+Transfer%2C+7th+Edition-p-9780470501979

Kouki, N., D'Agostino, D., & Vityi, A. (2025). Properties of Earth-to-Air Heat Exchangers (EAHE): Insights and perspectives based on system performance. Energies, 18(7), Article 1759. https://doi.org/10.3390/en18071759

Lee, K. W., Murid, A. H. M., Nasser, M. M. S., & Yeak, S. H. (2025). Fast implementation of generalized Koebe's iterative method. Mathematics, 13(12), Article 1920. https://doi.org/10.3390/math13121920

Li, D. (2025). A method of numerical conformal mapping of bounded multiply connected regions with rectilinear slit onto the first category canonical slit domains. AIMS Mathematics, 10(4), 9044-9073. https://doi.org/10.3934/math.2025388

Logan, J. D. (2015). Applied partial differential equations (3rd ed.). Springer. https://doi.org/10.1007/978-3-319-12493-3

Ma, Y., Liu, J., Li, L., Zhang, J., & Wang, X. (2024). Analysis of the heat transfer performance of a buried pipe in the heating season based on field testing. Energies, 17(21), Article 5466. https://doi.org/10.3390/en17215466

Müller, S., Bott, C., Schmitt, D., Bayer, P., & Schrag, T. (2026). Understanding buried dynamics: The relevance of pipe-ground interaction in thermal networks. Renewable and Sustainable Energy Reviews, 239, Article 117114. https://doi.org/10.1016/j.rser.2026.117114

Naqos, S., Murid, A. H. M., Nasser, M. M. S., & Yeak, S. H. (2024). Computing the Dirichlet-to-Neumann map via an integral equation with the adjoint generalized Neumann kernel. Partial Differential Equations in Applied Mathematics, 12, Article 100967. https://doi.org/10.1016/j.padiff.2024.100967

Nehari, Z. (1975). Conformal mapping. Dover Publications. https://store.doverpublications.com/products/9780486611373

Nield, D. A., & Bejan, A. (2017). Convection in porous media (5th ed.). Springer. https://doi.org/10.1007/978-3-319-49562-0

Olver, F. W. J., Lozier, D. W., Boisvert, R. F., & Clark, C. W. (Eds.). (2010). NIST handbook of mathematical functions. Cambridge University Press. https://dlmf.nist.gov/

Ozisik, M. N. (1993). Heat conduction (2nd ed.). Wiley. https://www.wiley.com/en-us/Heat+Conduction%2C+2nd+Edition-p-9780471532569

Qasim, H. H., Alshara, A. K., & Abood, F. A. (2024). Simulation of the effect of soil temperature on Earth-Air Heat Exchanger behavior. Basrah Journal for Engineering Sciences, 24(2), 12-23. https://doi.org/10.33971/bjes.24.2.3

Quarteroni, A., Sacco, R., & Saleri, F. (2010). Numerical mathematics (2nd ed.). Springer. https://doi.org/10.1007/b98885

Ramírez-Dolores, C., Molina-García, A., & Serrano-Tovar, T. (2024). Experimental evaluation of a heat exchanger for different underground configurations. International Journal of Energy and Environmental Engineering. https://doi.org/10.1007/s41939-024-00460-0

Ransford, T. (1995). Potential theory in the complex plane. Cambridge University Press. https://doi.org/10.1017/CBO9780511623776

Saleh, A. A. M. (2014). Energy saving of heat gain by using buried pipe inside a roof. Al-Khwarizmi Engineering Journal, 11(1), 32-39. https://alkej.uobaghdad.edu.iq/index.php/alkej/article/view/212

Salilih, E. M., Birhane, Y. T., & Fanta, S. W. (2024). Study of the transient heat transfer of a single-U-tube ground heat exchanger. Processes, 12(12), Article 2867. https://doi.org/10.3390/pr12122867

Shan, Y., & Lu, Y. (2025). An integral equation method in conformal mapping of regions with circular slit. Results in Applied Mathematics, 26, Article 100577. https://doi.org/10.1016/j.rinam.2025.100577

Trefethen, L. N., & Bau, D. (1997). Numerical linear algebra. SIAM. https://doi.org/10.1137/1.9780898719574

Wang, X., Zhou, Y., Yao, W., Xia, Y., Xu, T., Yang, H., Xie, H., & Gao, W. (2024). The challenge of the ground heat exchangers: A review of heat transfer efficiency. Energy Conversion and Management, 302, Article 118115. https://doi.org/10.1016/j.enconman.2024.118115

Zhang, L.-P., Li, Z.-C., Huang, H.-T., Lee, M.-G., & Kazakov, A. L. (2025). Study on discrete null-field equation methods for bounded simply connected domains: Better locations of source nodes. Mathematics, 13(1), Article 131. https://doi.org/10.3390/math13010131

Zhu, H. (2024). Numerical simulation of temperature field around buried heat exchangers under heat and seepage coupling. Thermal Science. https://doi.org/10.2298/TSCI2402441Z